UC Berkeley
UC Berkeley Previously Published Works

Title

Coupled polarization and nanodomain evolution underpins large electromechanical responses in relaxors

Permalink

https://escholarship.org/uc/item/7xg9043m

Journal

Nature Physics, 18(12)

ISSN

1745-2473

Authors

Kim, Jieun
Kumar, Abinash
Qi, Yubo
et al.

Publication Date

2022-12-01

DOI

10.1038/s41567-022-01773-y

Peer reviewed

Coupled polarization and nanodomain evolution underpins large electromechanical responses in relaxors

Check for updates

Jieun Kim [1,8], **Abinash Kumar** [2,8], **Yubo Qi** [3,8], **Hiroyuki Takenaka** [4], **Philip J. Ryan** [5], **Derek Meyers** [6], **Jong-Woo Kim** [5], **Abel Fernandez** [1,7], **Zishen Tian** [1], **Andrew M. Rappe** [3], **James M. LeBeau** [2] and **Lane W. Martin** [1,7] ✉

Understanding the evolution and role of nanoscale polar structures during polarization rotation in relaxor ferroelectrics is a long-standing challenge in materials science and condensed-matter physics. These nanoscale polar structures are characterized by polar nanodomains, which are believed to play a key role in enabling the large susceptibilities of relaxors. Using epitaxial strain, we stabilize the intermediate step during polarization rotation in epitaxial films of a prototypical relaxor and study the co-evolution of polarization and polar nanodomains. Our multimodal approach allows for a detailed examination of correlations between polarization and polar nanodomains; illuminates the effect of local chemistry, strain and electric field on their co-evolution; and reveals the underappreciated role of strain in enabling the large electromechanical coupling in relaxors. As the strain increases, the competition between chemistry-driven disorder and strain-driven order of the polar units intensifies, which is manifested in the coexistence of inclined and elongated polar nanodomains in the intermediate step of polarization rotation. Our findings establish that structural transitions between polar nanodomain configurations underpins the polarization rotation and large electromechanical coupling of relaxors.

The discovery of ultrahigh piezoelectricity in [001]-oriented single-crystal relaxors twenty-five years ago[1] sparked intense efforts to elucidate the origin of this large piezoelectric effect. Such large effects benefit from the ease of polarization rotation from rhombohedral to tetragonal symmetries near a morphotropic phase boundary or supercritical state[1–5]. Although early studies revealed such polarization rotation as a plausible mechanism to explain the observed effects, the nature of diffraction experiments used to extract this

information (averaged over many ($\geq 10^{12}$) unit cells) also obscured potential (simultaneous) mesoscopic mechanisms. Understanding such mesoscopic phenomena is particularly important for systems where the local disorder governs physical properties[6]. This is especially true in relaxors where nanoscale polar structures form by the spontaneous short-range correlation of dipoles over just a few nanometres (corresponding to $\approx 10^4$ unit cells) and are believed to play a dominant role in facilitating polarization rotation[7,8]. For brevity, hereafter, we

[1]Department of Materials Science and Engineering, University of California, Berkeley, CA, USA. [2]Department of Materials Science and Engineering, Massachusetts Institute of Technology, Cambridge, MA, USA. [3]Department of Chemistry, University of Pennsylvania, Philadelphia, PA, USA. [4]Department of Chemistry and Biochemistry, University of California, Santa Cruz, CA, USA. [5]Advanced Photon Source, Argonne National Laboratory, Argonne, IL, USA. [6]Department of Physics, Oklahoma State University, Stillwater, OK, USA. [7]Materials Sciences Division, Lawrence Berkeley National Laboratory, Berkeley, CA, USA. [8]These authors contributed equally: Jieun Kim, Abinash Kumar, Yubo Qi. ✉e-mail: lwmartin@berkeley.edu

refer to such nanoscale polar structures as polar nanodomains (PNDs). The relationship of PNDs and polarization rotation has been extensively discussed in various frameworks including those exploring adaptive phase theory, lattice softening, phonon localization, the concept of a morphotropic relaxor boundary and collinear domain structures[7–13]. But despite such efforts, the evolution and exact role of PNDs during polarization rotation remains to be fully understood. The challenge lies in characterizing the PNDs as the polarization rotates across different characteristic stages under external perturbations (for example, electric field and mechanical stress).

To overcome this challenge, we use epitaxial strain to stabilize the different stages of polarization rotation in the prototypical relaxor $0.68PbMg_{1/3}Nb_{2/3}O_3$-$0.32PbTiO_3$ (PMN-PT), and then apply a combination of real- and reciprocal-space experimental probes and molecular-dynamics simulations, including *in operando* hard X-ray diffraction (XRD) studies of both Bragg and diffuse scattering, to simultaneously interrogate the unit-cell and mesoscale structures. In turn, this multimodal approach allows for the detailed examination of correlations between polarization and PNDs and the effect of local chemistry, strain and electric field on their co-evolution and reveals the underappreciated role of strain in enabling the large electromechanical coupling in relaxors. It is found that as the strain increases, the competition between chemistry-driven disorder and strain-driven order of the polar units intensifies, which is manifested in the coexistence of inclined and elongated PNDs in the intermediate step of polarization rotation. Our findings establish that the structural transitions between PND configuration underpins the polarization rotation and large electromechanical coupling of relaxors.

Results

Synthesis of thin-film heterostructures

We focus on 55 nm PMN-PT/25 nm $Ba_{0.5}Sr_{0.5}RuO_3$ (BSRO)/$NdScO_3$ (NSO), $Nd_{0.5}Sm_{0.5}ScO_3$ (NSSO) and $SmScO_3$ (SSO) (110) heterostructures synthesized via pulsed-laser deposition (Methods). The lattice mismatch between PMN-PT and the different substrates gives rise to epitaxial compressive strains of −0.50%, −0.75% and −1.00% for heterostructures grown on NSO, NSSO and SSO substrates, respectively; the heterostructures will henceforth be referred to as the −0.50%, −0.75% and −1.00% heterostructures. Laboratory-based θ–2θ XRD linescans, rocking curves and asymmetric reciprocal-space mapping (RSM) studies (Methods) confirm that all the heterostructures are single phase, highly crystalline and coherently strained to the substrates (Supplementary Fig. 1).

Diffuse-scattering experiments

We examined diffuse scattering via synchrotron-based three-dimensional (3D) RSM studies (Methods). Diffuse scattering directly probes nanoscale inhomogeneities[14–17] and is commonly used to study the structure of PNDs. Previous studies on epitaxial thin films[18] revealed butterfly-shaped diffuse-scattering patterns (matching bulk measurements[19–21]) in −0.50% heterostructures, which originate from inclined PNDs with low-angle (≈55°) domain walls. The butterfly-shaped diffuse-scattering patterns are replaced by disc-shaped patterns in −1.00% heterostructures, which originate from elongated PNDs with high-angle (≈135°) domain walls. According to the polarization rotation mechanism[2,3], PMN-PT evolves from a rhombohedral (R) to an M_A-type monoclinic to a M_C-type monoclinic to a tetragonal (T) phase with increasing electric field along the [001] (Fig. 1a); here M_A and M_C are piezoelectrically distorted monoclinic forms of the parent R and T phases within the (110) and (100), respectively. We refer to electric-field-induced phase transitions from R to M_A, M_A to M_C and M_C to T as steps A, B and C, respectively[1,2]. As such, −0.5% (−1.0%) heterostructures represent an epitaxially stabilized representation of step A (C), where the macroscopic phases are predominantly composed of R and M_A (T and M_C) (Fig. 1b). Steps A and C are bridged by step B, where the electric-field-induced strain rises abruptly, indicating an

electric-field-induced first-order phase transition[22]. Consequently, unveiling the exact diffuse-scattering patterns corresponding to the PND structure in step B can greatly advance our understanding of the role of PNDs during polarization rotation. One may expect, similar to the first-order phase transition of macroscopic phases from R to T, a first-order structural transition for PNDs from inclined to elongated shape, which implies that step B may exhibit a mixture of butterfly and disc-shaped diffuse-scattering patterns rather than a smeared diffuse-scattering pattern. To test this hypothesis, we performed 3D RSM studies of −0.75% heterostructures about the PMN-PT 001 diffraction condition (Fig. 1c and Methods). We observe that −0.75% heterostructures possess diffuse-scattering patterns composed of a mixture of butterfly and disc-shaped features. Two-dimensional (2D) K–L (Fig. 1d) and H–K (Supplementary Fig. 2) cuts of the 3D RSM data reinforce the observation of coexisting butterfly and disc-shaped diffuse-scattering patterns. These coexisting diffuse-scattering patterns are intriguing and indicate different PND configurations may coexist in step B. Observations from diffuse scattering alone, however, are not sufficient to draw an accurate real-space model of PND evolution since diffuse scattering only contains two-body information. In other words, it is necessary to build a model and then confirm it by direct real-space imaging techniques.

Molecular-dynamics simulations

We performed molecular-dynamics simulations to probe the evolution of the domain structures and diffuse-scattering patterns and study the rotation of and correlation between the polar units (Methods). Here we focus on the −0.75% heterostructures, but 3D dipole patterns for the −0.50% and −1.00% heterostructures are provided for comparison (Supplementary Fig. 3). The simulated 3D-dipole patterns, exploring the polarization components along the three pseudocubic directions (P_{100}, P_{010} and P_{001}), for the −0.75% heterostructures show two main features. First, in the plane of the film (P_{100} and P_{010}; Fig. 2a), dipole patterns reveal PNDs inclined relative the principal <100>, similar to those observed in the −0.5% heterostructures where only butterfly-shaped diffuse-scattering patterns are observed[18] (Supplementary Fig. 3a). Second, out of the plane of the film (P_{001}; Fig. 2b), the dipole patterns show PNDs elongated along the principal [001], similar to those observed in −1.0% heterostructures where only disc-shaped diffuse-scattering patterns are observed (Supplementary Fig. 3g). Henceforth, we will refer to the PNDs originating from butterfly and disc-shaped diffuse-scattering patterns as inclined and elongated PNDs, respectively. The in-plane and out-of-plane dipole patterns are attributed to the weakening (strengthening) of the in-plane (out-of-plane) order due to the rotation of dipoles towards the out-of-plane directions under compressive strain (Supplementary Fig. 4). As a result, we observe hierarchical-domain structures[23], which are formed by multiple inclined PNDs with different in-plane orientations inside each elongated PND (Supplementary Fig. 3g). In turn, we can extract the corresponding diffuse-scattering patterns from these domain structures (Fig. 2c, right) and compare with experimentally observed diffuse-scattering patterns in the −0.75% heterostructures (Fig. 2c, left). The computational diffuse-scattering patterns exhibit diffuse intensities extending along the [011], $[0\bar{1}1]$, $[01\bar{1}]$ and $[0\bar{1}\bar{1}]$, which form the butterfly-shaped diffuse-scattering pattern, as well as intensities along the [010] and $[0\bar{1}0]$, which form the disc-shaped diffuse-scattering pattern. These results demonstrate that the computational diffuse-scattering patterns reproduce the key features of the experimental diffuse-scattering patterns for the −0.75% heterostructures. Consequently, we attribute the coexistence of the butterfly and disc-shaped diffuse-scattering patterns in the −0.75% heterostructures to such hierarchical-domain structures originating from the anisotropic correlations of in-plane- and out-of-plane-oriented dipoles under strain (Supplementary Figs. 5 and 6).
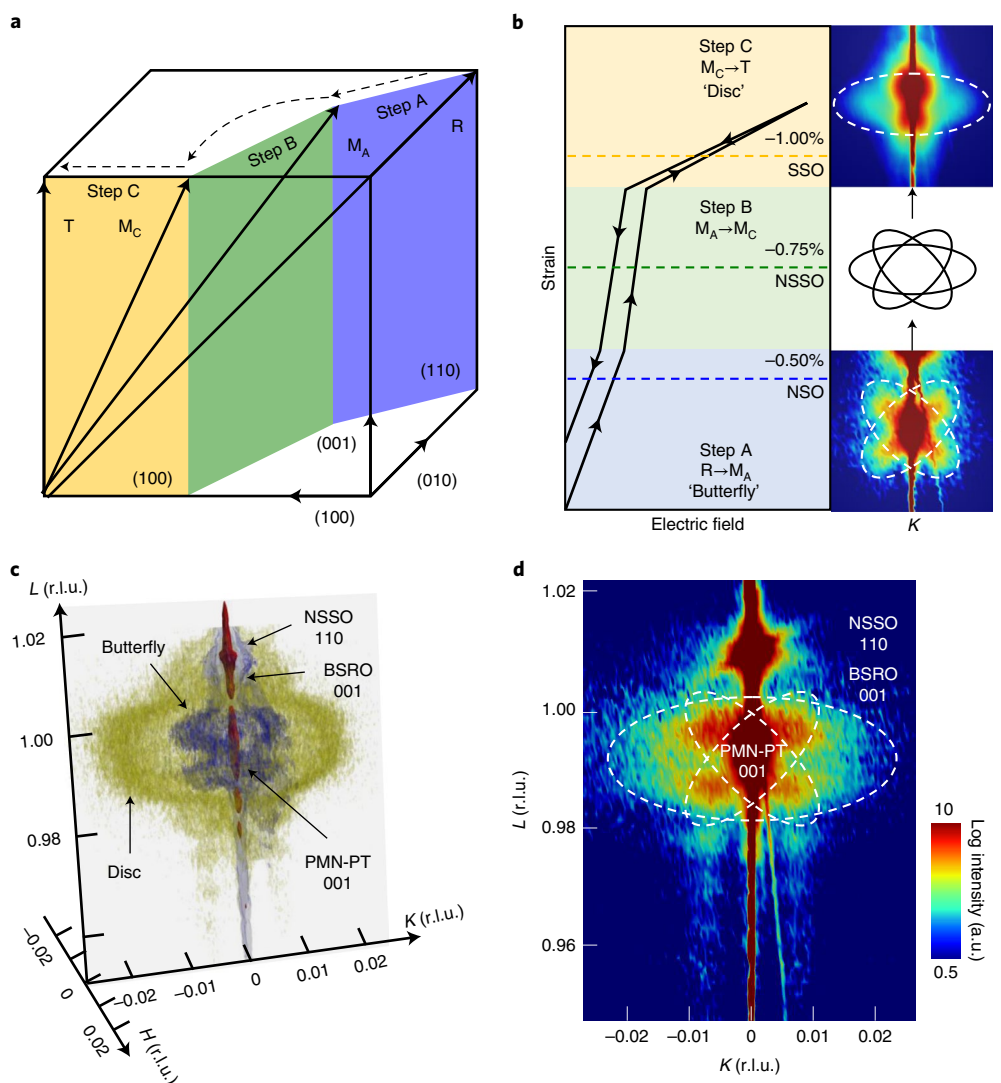
Fig. 1 | Reciprocal-space characterizations of the −0.75% heterostructures.
a, Schematic of the polarization rotation path in PMN-PT. Macroscopic symmetries (R, M_A, M_C, T) are assigned based on the polarization rotation path described elsewhere[5]. The solid arrows represent the direction of polarization vector for each macroscopic phase. At steps A and C, the straight dashed arrows represent the continuous rotation of polarization. At step B, the curved dashed arrow indicates a discontinuous jump of polarization from the (110) to the (100). **b**, Schematic of the strain–electric-field diagram and our model of associated diffuse-scattering patterns in different regions. The strain–electric-field diagram is based on macroscopic strain measurements reported in other work[5,22].

Diffuse-scattering patterns for steps A and C are reproduced from elsewhere[18]. The background colours in the diagram distinguish regions with different diffuse-scattering patterns along the strain axis, with corresponding diffuse-scattering patterns (indicated by dashed lines) reproduced from another study[18]. The diffuse-scattering pattern associated with step B is depicted based on the results from this study. **c**, Three-dimensional RSM studies about the PMN-PT 001-diffraction condition for the −0.75% heterostructures. **d**, Two-dimensional $K–L$ cut corresponding to the grey-shaded planes in **c**. In **c** and **d**, the coexistence of butterfly (blue) and disc-shaped (yellow) diffuse-scattering patterns from steps A and C can be clearly seen. 1 r.l.u. ≡ 1/4.03 Å.

The agreement between computational and experimental diffuse-scattering patterns also offers an opportunity to confirm the validity of the model by directly observing such domain structures in real space.

STEM

We performed annular dark-field (ADF) and integrated differential phase contrast (iDPC) measurements (collected simultaneously) with scanning transmission electron microscopy (STEM) to determine the structure and nanoscale polarization variation (Methods). Consistent with the diffraction studies, ADF-STEM shows that the PMN-PT films are epitaxially grown with the BSRO bottom electrode and NSSO substrate (Fig. 2d,e) and misfit dislocations are not observed. Furthermore, the in-plane and out-of-plane components of the projected polarization

(net displacement between the cation and anion columns in a unit cell determined using iDPC images) reveal the domain state of the strained PMN-PT (Supplementary Fig. 7). For −0.75% heterostructures, the domain pattern reveals substantial differences between the in-plane and out-of-plane polarization/displacement maps (Fig. 2f). Inclined PNDs, ≈12 nm long and ≈4 nm wide, are found in the in-plane polarization/displacement map (Fig. 2f, left), whereas the out-of-plane displacements exhibit stronger correlation where an ≈10-nm-thick downward polarization domain spans the image near the interface with the rest of the out-of-plane component pointing towards the surface (dotted lines along the [001]). Smaller PNDs are also found within the out-of-plane displacements as highlighted by the ellipses (Fig. 2f, right). To determine the effect of strain on the domain structure, projected polarization/net displacements maps are also investigated for the
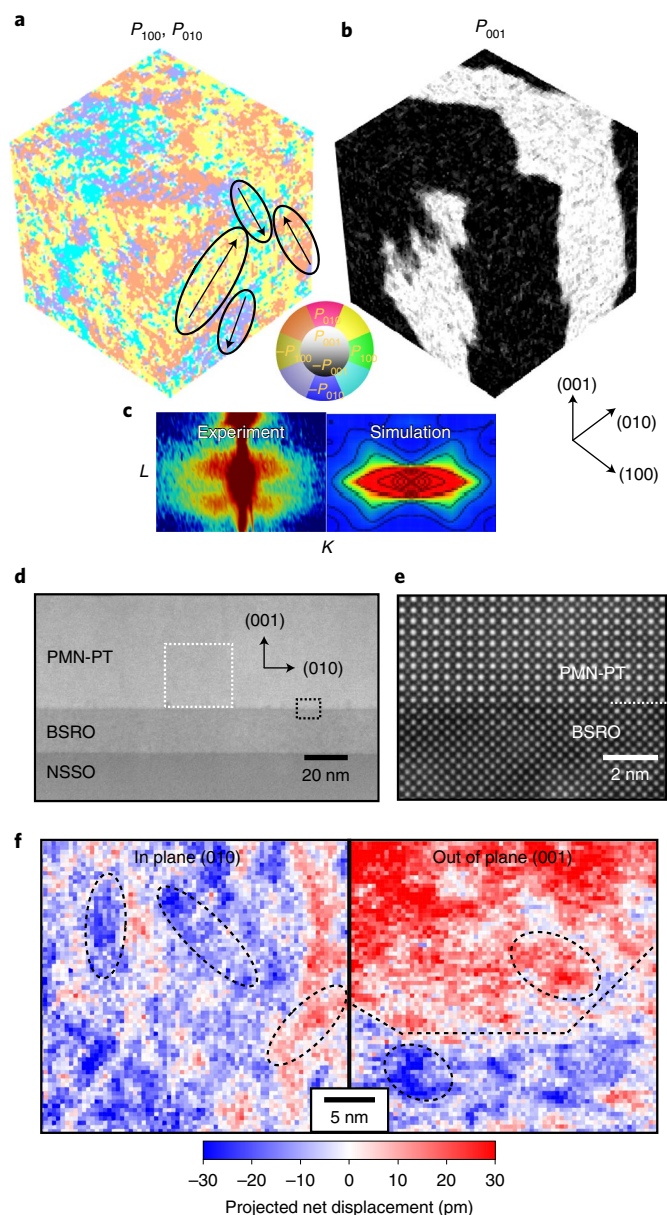
Fig. 2 | Real-space characterizations of the −0.75% heterostructures.
a,b, Snapshots of dipole patterns in the −0.75% heterostructures from molecular-dynamics simulations using a 72 × 72 × 72 supercell showing P_{100} and P_{010} (**a**) and P_{001} (**b**) polarization components. In **a**, the arrows and ellipses indicate PNDs. The intermediacy of the −0.75% heterostructures is evident from the resemblance of in-plane and out-of-plane dipole patterns to the −0.50% and −1.00% heterostructures and indicates that the merging of PNDs along the out-of-plane directions starts to occur before merging along the in-plane directions. **c**, $K–L$ cut of 3D RSM about the PMN-PT 001-diffraction condition and calculated diffuse-scattering patterns in the $K–L$ plane about the PMN-PT 002-diffraction condition. **d**, ADF-STEM overview of the film structure. **e**, Atomic-resolution ADF-STEM image from the PMN-PT/BSRO interface (black box in **d**). **f**, Projected polarization/net displacements in the map of the in-plane and out-of-plane directions from a cross section of the −0.75% heterostructure (white box in **d**). Each square represents the projected polarization of one unit cell. The presence of inclined PNDs within a uniform out-of-plane region is evident.

−0.5% and −1.0% heterostructures (Supplementary Fig. 7). Inclined PNDs are also found in the −0.5% heterostructures, where the domain walls also lie on the {011} and thus produce the butterfly-shaped diffuse-scattering patterns—an observation suggested by previous

theoretical calculations[17]. Out-of-plane projected polarization in the −0.5% heterostructures reveals domain structures with inclined PNDs with the major axes either along the [010] or rotated ≈45° with respect to the [010]. Horizontally aligned inclined PNDs are found (width, 1–2 nm) in the −0.5% heterostructures. With increasing strain, the inclined PNDs are found to combine and form elongated PNDs along the [001] with high-angle (≈135°) domain walls between them, as observed for the −0.75% and −1.00% heterostructures. These observations directly confirm that the out-of-plane component of polarization becomes dominant with increasing compressive strain, in agreement with the analysis of dipole orientations from molecular-dynamics simulations (Supplementary Fig. 4).

The local distortions in relaxors have also been found to be correlated with changes in the local distribution of constituent atoms[21,24]. To understand the effect of strain on the correlation between local distortions and chemistry, the average lead–lead distances around each *B*-site sublattice position (containing magnesium, niobium, or titanium in projection) are plotted with respect to its normalized intensity obtained from the chemically sensitive ADF images (Supplementary Fig. 8). Approximately 20,000 unit cells are used from each heterostructure for this analysis. Notably, for the −0.50% heterostructures, correlation is found between the normalized *B*-site sublattice intensity and the nearest-neighbour-like lead–lead distances with a Pearson correlation coefficient $r = 0.39$. As the strain increases, the correlation decreases ($r = 0.25$) for the −0.75% heterostructures, and there is essentially no correlation ($r = 0.16$) for the −1.00% heterostructures. This decrease in correlation between local chemistry and distortion indicates that strain dominates the lead displacements regardless of variation in local chemistry. The decoupling of lead displacements from local chemistry using strain, in turn, opens the door to re-examine the origin of large electromechanical coupling based on traditional compositional phase diagrams[21] and to directly observe how PND structures evolve during polarization rotation.

In operando μXRD of Bragg and diffuse scattering

To understand the relation of the observed changes in the PND structures to polarization rotation, we studied the dynamic, electric-field-driven evolution of the polarization and PND structures using *in operando* X-ray microdiffraction (μXRD)[25] (Methods). We measured both Bragg and diffuse scattering of the −0.50%, −0.75% and −1.00% heterostructures about the PMN-PT 00L diffraction conditions under an a.c. electric field (Fig. 3). The Bragg and diffuse scattering measure changes in the unit-cell structure/symmetry and PND structures, respectively. At zero electric field, the −0.50%, −0.75% and −1.00% heterostructures exhibit a mixture of two phases, which we attribute to the R + M_A, M_A + M_C and M_C + T mixtures, respectively (Fig. 3a–c). During the initial increase in electric field from 0 to 400 kV cm⁻¹ for the −0.50% (Fig. 3a) and −1.00% (Fig. 3c) heterostructures, the diffraction peaks arising from the R and T phases (corresponding to the smallest and largest out-of-plane lattice parameters, respectively) do not show noticeable differences, indicating that the out-of-plane lattice parameters of the R and T phase are mostly insensitive to electric field[26]. In contrast, the diffraction peaks corresponding to the M_A (M_C) phase in the −0.5% (−1.0%) heterostructures show immediate and nearly continuous shifts to lower L (corresponding to an expansion of the out-of-plane lattice parameters) with an increasing electric field; effects that are expected from the larger degrees of freedom in the M_A and M_C phases compared with the R and T phases[27]. Above 400 kV cm⁻¹, the M_A peak in the −0.5% heterostructures continues to shift to lower L, but a first-order-like transition from the M_C to T phase is observed in the −1.0% heterostructures. In the −0.75% heterostructures (Fig. 3b), both M_A and M_C peaks shift to lower L with an increasing electric field from 0 to 400 kV cm⁻¹, where an abrupt transition from the M_A to M_C phase is observed[28]. Above 400 kV cm⁻¹, the M_C peak continues to shift to lower L, whereas the remaining metastable M_A
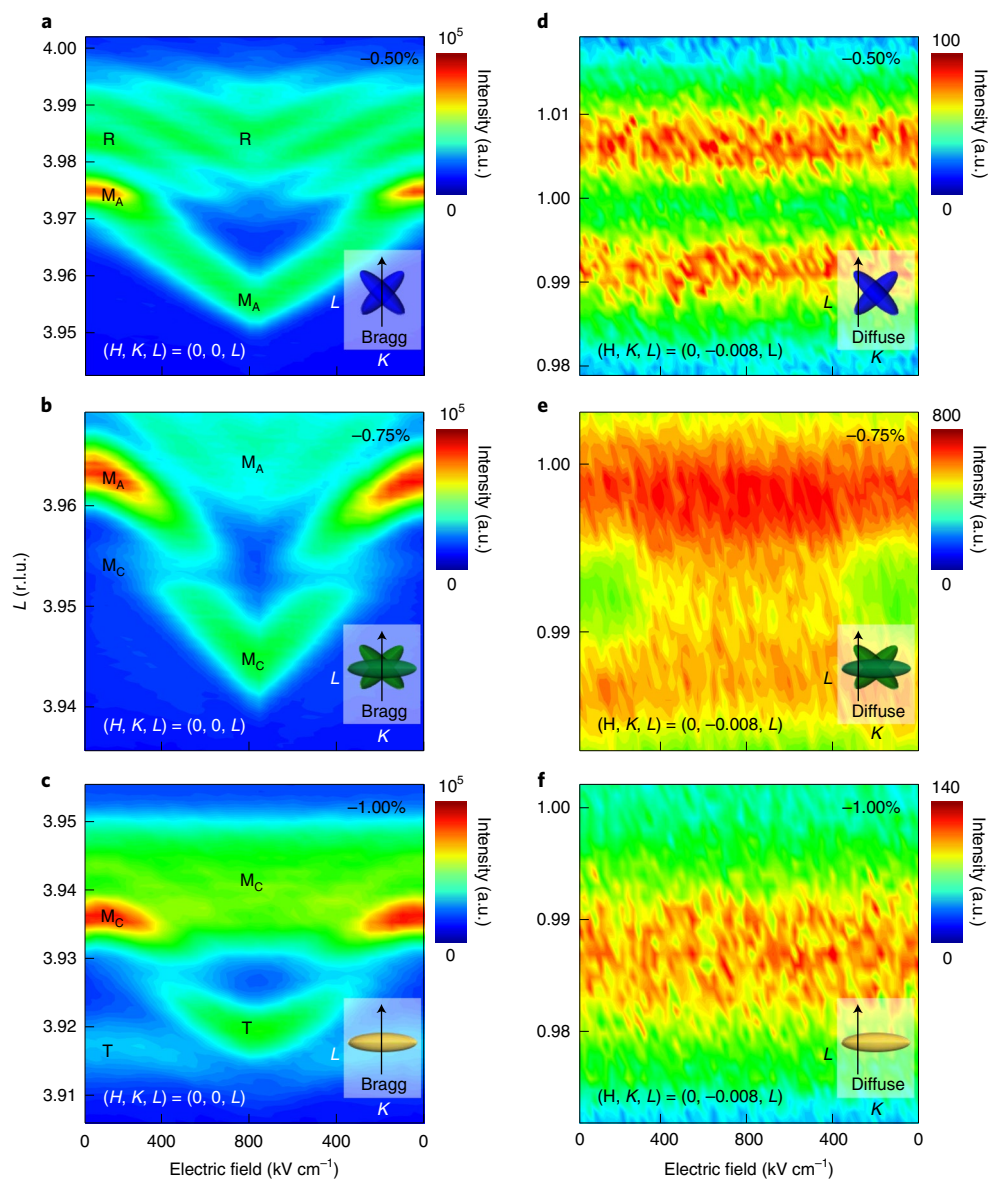
Fig. 3 | *In operando* µXRD under applied electric field. a–c, Measured X-ray intensities in the Bragg-scattering conditions as a function of the reciprocal-space position $(0, 0, L)$ and the electric field along the [001] for −0.50% (**a**), −0.75% (**b**) and −1.00% (**c**) heterostructures. **d–f**, Measured X-ray intensities in the diffuse-scattering conditions as a function of the reciprocal-space position $(0, −0.008, L)$ and the electric field along the [001] for −0.50% (**d**), −0.75% (**e**) and −1.00% (**f**) heterostructures. The schematic on the left-hand side shows the direction of scans relative to the diffuse-scattering patterns. In all the cases, the Bragg peak is at the centre of the diffuse-scattering pattern. The coincidence of the M_A-to-M_C transition and abrupt increase in diffuse-scattering intensity is evident in **b** and **d**.

peak shows negligible variations with the increasing electric field. The Bragg scattering results are in good agreement with the macroscopic strain measurements on single-crystal relaxors[22].

The diffuse scattering for the −0.5% heterostructures (Fig. 3d) reveals two peaks at zero electric field (arising from the butterfly-shaped diffuse-scattering pattern) and the −1.0% heterostructures (Fig. 3f) reveal one peak at zero electric field (arising from the disc-shaped diffuse-scattering patterns). No obvious changes in the diffuse-scattering patterns for the −0.5% and −1.0% heterostructures are observed with an increasing electric field, suggesting that steps A and C do not involve significant changes in the PND structures[29]. By contrast, the diffuse scattering for the −0.75% heterostructures reveals an abrupt increase in diffuse-scattering intensity near the disc-shaped diffuse-scattering pattern at 400 kV cm⁻¹ (Fig. 3e), indicating that the M_A-to-M_C transition is

accompanied by structural transitions of the PNDs from the inclined to elongated shape.

The electric-field-induced strains are extracted by fitting the X-ray intensity profiles (Methods) and reveal that the −0.75% heterostructures show a sharp increase in strain above 400 kV cm⁻¹ (Fig. 4a), where the M_A-to-M_C transition occurs, consistent with the strain–electric-field diagram of single-crystal relaxors[1,5,22,28]. Additional diffuse-scattering measurements performed along the reciprocal lattice vector K reveal that the correlation lengths along the in-plane directions decrease from ≈13.3 to ≈9.7 nm when the M_A-to-M_C transition occurs (Fig. 4b and Methods). The decrease in the in-plane correlation length suggests that the change in the PND structure from the inclined to elongated shape is driven by the rotation of the PNDs towards the electric field before eventual merging increases the average size of the PNDs[18,30].
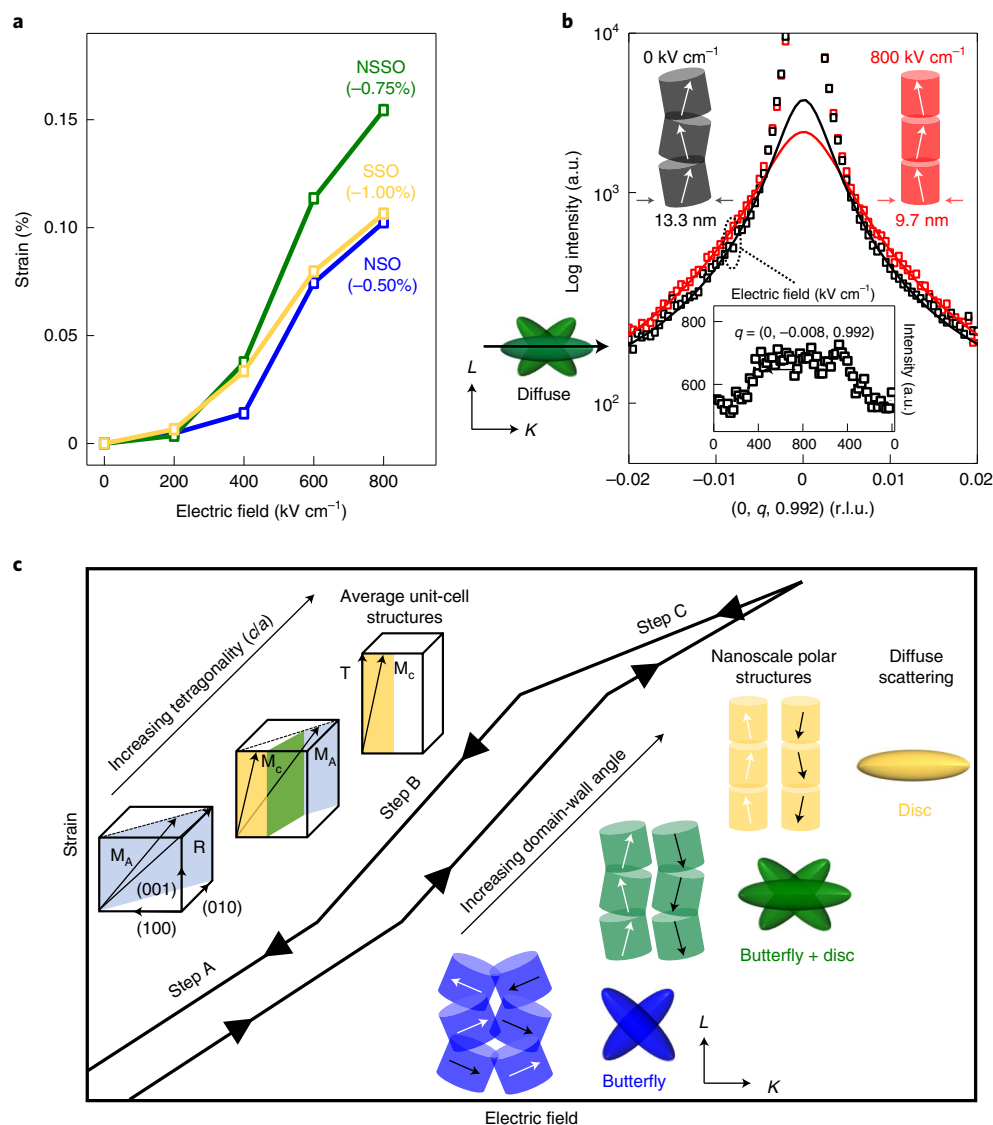
Fig. 4 | Analysis of *in operando* µXRD under applied electric field. a, Strain as a function of electric field determined from Voigt fitting of the Bragg-scattering-intensity profiles. **b**, Measured X-ray intensities in the diffuse-scattering conditions as a function of reciprocal-space position (0, K, 0.992) for zero electric field and 0.8 MV cm^{-1} of electric field along the [001] for −0.75% heterostructures. The empty circles are data points and solid lines are fits to the diffuse-scattering parts. The inset shows the schematic of the nanodomain structures under zero and maximum electric fields and their average correlation lengths determined from Lorentzian fitting of the diffuse-scattering-intensity profiles. The inset shows the electric-field dependence of a fixed point in the reciprocal space (0, −0.008, 0.992). The sharp increase in the diffuse-scattering intensities around 0.4 MV cm^{-1} corresponds to the transition from the inclined to elongated PND. **c**, Schematic of the relationship between strain–electric-field diagram of PMN-PT, average unit-cell structures, nanoscale polar structures and diffuse scattering. The bottom, middle and top rows correspond to steps A, B and C, respectively. On the right-hand side, the black and white solid arrows correspond to the average polarization directions in each nanodomain.

Discussion

We offer a comprehensive picture of the evolution of the macroscopic phases and PND structures (Fig. 4c). As the unit cells become more tetragonally distorted under an electric field (that is, contracting (elongating) along the in-plane (out-of-plane) directions), inclined PNDs rotate towards the electric field and become elongated PNDs due to the weakening (strengthening) of the in-plane (out-of-plane) order. Evidently, the abrupt transition of the structure/symmetry from M_A to M_C in step B simultaneously occurs with an abrupt transition of the PND structures from inclined to elongated shapes.

Moreover, epitaxial strain has been used to stabilize the intermediate step in polarization rotation that separates the inclined and elongated PND structures in PMN-PT. Using multiple real- and reciprocal-space probes, coexisting diffuse-scattering patterns were identified as the mesoscopic structural signature of the intermediate step in polarization rotation. In step B, the coexistence of different PND configurations enhances the local structural disorder and leads to a highly susceptible state[31]. The observation of coexisting PND structures in step B demystifies the role played by PNDs in the enhanced electromechanical coupling of relaxors. Specifically, these results suggest that the structural transitions of PNDs and individual unit cells simultaneously occur during polarization rotation. It is argued that polarization rotation in PMN-PT should be thought of as an emergent phenomenon where dipoles within each PND rotate together as a unit. In addition, the supercritical state under an electric field, in which an external electric field induces an unusual inverse transition[32] from a more ordered (ferroelectric) state into a disordered (supercritical) state[4,8], is a manifestation of the enhanced local structural disorder

induced by the coexisting PND configurations in step B. The enhanced local structural disorder lowers the energy barrier between different PND structures, which consequently reduces the energy barrier for macroscopic polarization rotation. At the same time, the large piezoelectric constant d_{33} in step B (ref. [1]) is due to the enhanced local structural disorder and phase instabilities[7,10] when step B is reached by electric-field-induced strains[33] (or conversely by mechanical stress[34]).

These observations also help explain how the substitution of small rare-earth elements in lead sites, which induces tetragonal strains in the lattice[35], can improve the relaxor performance as this alloying essentially moves step B closer to zero electric field by stabilizing elongated PNDs, thereby enhancing the competition between inclined and elongated PNDs at a low field. Finally, the piezoelectric and dielectric constants are maximized at the maximum of diffuse-scattering intensity[21,36]. The enhanced diffuse-scattering intensities with increasing $PbTiO_3$ concentration and the reduction in indentation along the <100> of the butterfly-shaped diffuse-scattering pattern near the PMN-PT 100-diffraction condition are due to the growth of disc-shaped diffuse-scattering patterns along the <100>, which can be attributed to the increasing tetragonal strains by $PbTiO_3$ addition. These results are also consistent with the recently reported domain-engineered ferroelectric $BiFeO_3$ where the strain–electric-field diagram exhibits three characteristic steps[37]. It is, thus, proposed that relaxors with enhanced performance could be found by enhancing competition across multiple length scales.

Online content

Any methods, additional references, Nature Research reporting summaries, source data, extended data, supplementary information, acknowledgements, peer review information; details of author contributions and competing interests; and statements of data and code availability are available at https://doi.org/10.1038/s41567-022-01773-y.

References

1. Park, S.-E. & Shrout, T. R. Ultrahigh strain and piezoelectric behavior in relaxor based ferroelectric single crystals. *J. Appl. Phys.* **82**, 1804–1811 (1997).
2. Fu, H. & Cohen, R. E. Polarization rotation mechanism for ultrahigh electromechanical response in single-crystal piezoelectrics. *Nature* **403**, 281–283 (2000).
3. Bai, F. et al. X-ray and neutron diffraction investigations of the structural phase transformation sequence under electric field in 0.7Pb($Mg_{1/3}Nb_{2/3}$)-0.3$PbTiO_3$ crystal. *J. Appl. Phys.* **96**, 1620–1627 (2004).
4. Kutnjak, Z., Petzelt, J. & Blinc, R. The giant electromechanical response in ferroelectric relaxors as a critical phenomenon. *Nature* **441**, 956–959 (2006).
5. Noheda, B. et al. Polarization rotation via a monoclinic phase in the piezoelectric 92% $PbZn_{1/3}Nb_{2/3}O_3$-8% $PbTiO_3$. *Phys. Rev. Lett.* **86**, 3891–3894 (2001).
6. Wall, S. et al. Ultrafast disordering of vanadium dimers in photoexcited VO_2. *Science* **362**, 572–576 (2018).
7. Xu, G., Wen, J., Stock, C. & Gehring, P. M. Phase instability induced by polar nanoregions in a relaxor ferroelectric system. *Nat. Mater.* **7**, 562–566 (2008).
8. Li, F. et al. The origin of ultrahigh piezoelectricity in relaxor-ferroelectric solid solution crystals. *Nat. Commun.* **7**, 13807 (2016).
9. Jin, Y. M., Wang, Y. U., Khachaturyan, A. G., Li, J. F. & Viehland, D. Adaptive ferroelectric states in systems with low domain wall energy: tetragonal microdomains. *J. Appl. Phys.* **94**, 3629–3640 (2003).
10. Otoničar, M. et al. Connecting the multiscale structure with macroscopic response of relaxor ferroelectrics. *Adv. Funct. Mater.* **30**, 2006823 (2020).
11. Manley, M., Lynn, J., Abernathy, D. & Specht, E. Phonon localization drives polar nanoregions in a relaxor ferroelectric. *Nat. Commun.* **5**, 3683 (2013).
12. Manley, M. E. et al. Giant electromechanical coupling of relaxor ferroelectrics controlled by polar nanoregion vibrations. *Sci. Adv.* **2**, e1501814 (2015).
13. Yang, Y. et al. Morphotropic relaxor boundary in a relaxor system showing enhancement of electrostrain and dielectric permittivity. *Phys. Rev. Lett.* **123**, 137601 (2019).
14. Welberry, T. R. Diffuse scattering and Monte Carlo studies of relaxor ferroelectrics. *Metall. Mater. Trans.* **39**, 3170–3178 (2008).
15. Goossens, D. Diffuse scattering from lead-containing ferroelectric perovskite oxides. *ISRN Mater. Sci.* **2013**, 107178 (2013).
16. Bosak, A., Chernyshov, D., Vakhrushev, S. & Krisch, M. Diffuse scattering in relaxor ferroelectrics: true three-dimensional mapping, experimental artefacts and modelling. *Acta Crystallogr. A Found. Adv.* **68**, 117–123 (2012).
17. Paściak, M., Wołcyrz, M. & Pietraszko, A. Interpretation of the diffuse scattering in Pb-based relaxor ferroelectrics in terms of three-dimensional nanodomains of the ⟨110⟩-directed relative interdomain atomic shifts. *Phys. Rev. B* **76**, 014117 (2007).
18. Kim, J. et al. Epitaxial strain control of relaxor ferroelectric phase evolution. *Adv. Mater.* **31**, 1901060 (2019).
19. Xu, G., Zhong, Z., Hiraka, H. & Shirane, G. Three-dimensional mapping of diffuse scattering in Pb($Zn_{1/3}Nb_{2/3}$)O_3-x$PbTiO_3$. *Phys. Rev. B* **70**, 174109 (2004).
20. Takenaka, H., Grinberg, I., Liu, S. & Rappe, A. M. Slush-like polar structures in single-crystal relaxors. *Nature* **546**, 391–395 (2017).
21. Krogstad, M. J. et al. The relation of local order to material properties in relaxor ferroelectrics. *Nat. Mater.* **17**, 718–724 (2018).
22. Davis, M., Damjanovic, D. & Setter, N. Electric-field-, temperature-, and stress-induced phase transitions in relaxor ferroelectric single crystals. *Phys. Rev. B* **73**, 014115 (2006).
23. Sato, Y., Hirayama, T. & Ikuhara, Y. Real-time direct observations of polarization reversal in a piezoelectric crystal: Pb($Mg_{1/3}Nb_{2/3}$)O_3-$PbTiO_3$ studied via in situ electrical biasing transmission electron microscopy. *Phys. Rev. Lett.* **107**, 187601 (2011).
24. Kumar, A. et al. Atomic-resolution electron microscopy of nanoscale local structure in lead-based relaxor ferroelectrics. *Nat. Mater.* **20**, 62–67 (2021).
25. Kim, J. et al. Frequency-dependent suppression of field-induced polarization rotation in relaxor ferroelectric thin films. *Matter* **4**, 2367–2377 (2021).
26. Guo, R. et al. Origin of the high piezoelectric response in $PbZr_{1-x}Ti_xO_3$. *Phys. Rev. Lett.* **84**, 5423–5426 (2000).
27. Davis, M. Picturing the elephant: giant piezoelectric activity and the monoclinic phases of relaxor-ferroelectric single crystals. *J. Electroceram.* **19**, 25–47 (2007).
28. Ohwada, K. et al. Neutron diffraction study of the irreversible R–M_A–M_C phase transition in single crystal Pb[($Zn_{1/3}Nb_{2/3}$)$_{1-x}$Ti$_x$]O_3. *J. Phys. Soc. Jpn* **70**, 2778–2783 (2001).
29. Wen, J., Xu, G., Stock, C. & Gehring, P. M. Response of polar nanoregions in 68%Pb($Mg_{1/3}Nb_{2/3}$)O_3-32%$PbTiO_3$ to a [001] electric field. *Appl. Phys. Lett.* **93**, 082901 (2008).
30. Prosandeev, S., Wang, D. & Bellaiche, L. Properties of epitaxial films made of relaxor ferroelectrics. *Phys. Rev. Lett.* **111**, 247602 (2013).
31. Li, F., Zhang, S., Damjanovic, D., Chen, L. & Shrout, T. R. Local structural heterogeneity and electromechanical responses of ferroelectrics: learning from relaxor ferroelectrics. *Adv. Funct. Mater.* **28**, 1801504 (2018).
32. Nahas, Y. et al. Inverse transition of labyrinthine domain patterns in ferroelectric thin films. *Nature* **577**, 47–51 (2020).

33. Kisi, E. H., Piltz, R. O., Forrester, J. S. & Howard, C. J. The giant piezoelectric effect: electric field induced monoclinic phase or piezoelectric distortion of the rhombohedral parent? *J. Phys. Condens. Matter* **15**, 3631 (2003).

34. Janolin, P.-E., Dkhil, B., Davis, M., Damjanovic, D. & Setter, N. Uniaxial-stress induced phase transitions in [001]C-poled $0.955Pb(Zn_{1/3}Nb_{2/3})O_3$–$0.045PbTiO_3$. *Appl. Phys. Lett.* **90**, 152907 (2007).

35. Li, F. et al. Giant piezoelectricity of Sm-doped $Pb(Mg_{1/3}Nb_{2/3})O_3$-$PbTiO_3$ single crystals. *Science* **364**, 264–268 (2019).

36. Matsuura, M. et al. Composition dependence of the diffuse scattering in the relaxor ferroelectric compound $(1-x)$ $Pb(Mg_{1/3}Nb_{2/3})O_3$–$xPbTiO_3 (0 \leq x \leq 0.40)$. *Phys. Rev. B* **74**, 144107 (2006).

37. Paull, O. et al. Anisotropic epitaxial stabilization of a low-symmetry ferroelectric with enhanced electromechanical response. *Nat. Mater.* **21**, 74–80 (2021).

Methods

Thin-film synthesis using pulsed-laser deposition

Pulsed-laser deposition using a KrF excimer laser (248 nm, LPX 300, Coherent) was used to grow 55 nm PMN-PT/25 nm BSRO heterostructures on NSO, NSSO and SSO (110) substrates (CrysTec). The PMN-PT growth was carried out at a heater temperature of 590 °C in a dynamic oxygen pressure of 200 mtorr with a laser fluence of 2.0 J cm^{-2} and a laser repetition rate of 2 Hz from a ceramic target (Praxair) of the same composition with 10% excess lead to compensate for lead loss during growth. The BSRO growth was carried out at a temperature of 800 °C in a dynamic oxygen pressure of 20 mtorr with a laser fluence of 1.8 J cm^{-2} and a laser repetition rate of 2 Hz from a ceramic target (Praxair) of the same composition. Following the growth, the samples were cooled to room temperature at 5 °C min^{-1} in a static oxygen pressure of 700 torr.

XRD

Laboratory-based XRD studies. To augment the data in the main text, symmetric X-ray θ–2θ linescans, rocking curves and 2D RSM studies were conducted with a high-resolution XRD system (X'Pert Pro2, PANalytical) for all the heterostructure variants in this study (Supplementary Fig. 1). All the PMN-PT films, regardless of strain state, reveal high-crystalline quality as indicated by the narrow full-width at half-maximum values (<0.06°), which are 6–10 times larger than those of the substrates. Asymmetric RSM studies show that for all the heterostructures, the in-plane lattice parameters of the PMN-PT and bottom-electrode BSRO films are found to match the in-plane lattice parameters of the underlying substrates, which proves that PMN-PT films in this study are coherently strained without any strain relaxation and have well-defined strain states. Avoiding strain relaxation is critical for diffuse-scattering measurements since the broadening of the main Bragg peaks due to strain relaxation dominates the diffuse scattering and obscures the diffuse scattering originating from true polar order.

Synchrotron-based XRD studies. Synchrotron-based X-ray 3D RSM studies were conducted using a Huber four-circle diffractometer and Pilatus 100K pixel detector with X-ray energy of 10 keV at the sector 33-BM-C beamline of the Advanced Photon Source at Argonne National Laboratory. To calculate the reciprocal lattice vectors (H, K, L), we used 4.03 Å for the pseudocubic lattice parameters of the unstrained bulk PMN-PT (1 r.l.u. ≡ 1/4.03 Å) throughout this work.

Extraction of correlation lengths from diffuse scattering. To examine the electric-field-induced changes in the correlation length, which is a measure of the average size of the local polar order, line profiles of the diffuse-scattering intensity (along the [010] for the −0.75% heterostructures) were fitted with a Lorentzian function as

$$I_{\mathrm{diff}} = \frac{I_0 \Gamma}{\pi(q^2 + \Gamma^2)}, \tag{1}$$

where I_0 is the integrated diffuse scattering intensity, Γ is the half-width at half-maximum of the Lorentzian profile and the inverse of ξ, and q is the length of the wavevector measured from the Bragg positions.

Device fabrication for synchrotron-based *in operando* μXRD. A multistep microfabrication process was designed and employed to produce devices that enable stable electrical contact during *in operando* measurements of the PMN-PT thin films (Supplementary Fig. 9). In the following, we provide details of the device fabrication process. First, 100 nm SrRuO$_3$ (SRO)/55 nm PMN-PT/25 nm BSRO/NSO, NSSO and SSO (110) heterostructures were grown via pulsed-laser deposition. Second, the heterostructures were spin coated with a photoresist. Third, the photoresist was patterned to be bar shaped by photolithography. Fourth, the sample was ion milled for a total depth of ≈300 nm over a 30 min period (≈10 nm min^{-1}) at a beam voltage of 300 V, acceleration

voltage of 45 V and beam current of 5 mA to completely remove the SRO/PMN-PT/BSRO layers outside the photoresist. Fifth, the remaining photoresist was patterned into circular shapes with a diameter of 50 μm. Sixth, the heterostructures were wet etched in 0.2 M NaIO$_4$ solution for 1 min to remove the SRO outside the photoresist, thus defining circular-SRO top electrodes. Seventh, a MgO layer was grown at room temperature under a dynamic oxygen pressure of 20 mtorr at a laser repetition rate of 15 Hz and laser fluence of 2.5 J cm^{-2} to serve as an insulating layer. Eighth, the photoresist was removed with acetone to expose the SRO top electrodes. Ninth, the heterostructures were spin coated with the photoresist for the second photolithography. Tenth, inverse patterns of external platinum contact pads were defined by photolithography. Eleventh, 80-nm-thick platinum was sputter deposited at room temperature and a target power of 100 W in a dynamic argon pressure of 2 mtorr. The photoresist was subsequently removed with acetone. The platinum contact pads were wire bonded to leaded chip carriers to apply an electric field along the [001]. An optical microscopy image of the actual devices is shown in Supplementary Fig. 9l.

Synchrotron-based *in operando* μXRD studies. *In operando* μXRD was conducted at room temperature using a Huber four-circle diffractometer and Pilatus 100K pixel detector with X-ray energy of 10 keV at beamline 6-ID-B at the Advanced Photon Source at Argonne National Laboratory. An electrical connection to the voltage source was made by soldering wires on the metal leads of the chip carrier after mounting the samples on the sample stage of the diffractometer. For the μXRD, a 25 μm pinhole was used to avoid overlap of the X-ray beam with the inactive region. The active device was aligned by rastering the sample in the in-plane directions with a step size less than 5 μm. After the alignment of the X-ray beam with the active device, the sample was aligned for the PMN-PT 004-diffraction condition for Bragg scattering and the 001-diffraction condition for diffuse scattering. For all *in operando* measurements, a triangular waveform was used to apply an a.c. voltage at 100 Hz. This waveform was matched with 64 bins to record the accumulated intensities at each voltage step. The 2D mapping of the reciprocal lattice vector versus electric field is obtained by cycling the electric field at a fixed position in the reciprocal space before moving to the next position. At each position, the intensities were collected for at least 30 s to ensure sufficient statistics. The step size of the scans was set to be less than 0.0005 r.l.u. to acquire high-resolution data. For Bragg scattering, the heterostructures were scanned along L with H and K fixed at 0 r.l.u. about the PMN-PT 004-diffraction condition (Fig. 3a–c). We identify the presence of four peaks across the heterostructures studied here. The centres of these four peaks are located at around 3.985, 3.975, 3.955 and 3.915 r.l.u. Based on previous reports, we assign the R, M$_A$, M$_C$ and T phases to these peaks in a decreasing order in L (that is, in an increasing order in the c lattice parameter), which is justified by the fact that the c lattice parameter only increases during polarization rotation from R to T. From the L versus electric field (Fig. 3a–c) data, it is evident that the peaks corresponding to M$_A$ and M$_C$ have large variations with electric field, whereas the peaks corresponding to R and T do not show significant variations. These observations are consistent with the fact that M$_A$ and M$_C$ have large degrees of freedom since the polarization vectors are only constrained to lie within the (110) and (100), respectively, whereas R and T have limited degrees of freedom since the polarization vectors are constrained to lie only along <111> and <001>, respectively.

To estimate the electric-field-induced strain (Fig. 4a), the diffraction profiles were fitted with a standard Voigt function, which is the convolution of Gaussian and Lorentzian functions. For diffuse scattering, the heterostructures were scanned along L or K (Figs. 3d–f and 4b). All the heterostructures were first scanned along L with fixed $H = 0$ r.l.u. and $K = -0.008$ r.l.u. The K position and L range were determined from the 3D RSM data (Fig. 1c). We observed changes in the diffuse-scattering intensities only in the −0.75% heterostructures (Fig. 3d). An additional

diffuse-scattering scan was performed along K for the −0.75% hetero-structures (Fig. 4b) to measure the intensity profile along the direction of diffuse scattering where an increase in diffuse-scattering intensities was observed. For this scan, the L position was fixed at 0.992 r.l.u. so that the scan passes through the centre of the Bragg peak for the PMN-PT 001-diffraction condition. The diffuse part of each scan was fitted to Lorentzian profiles to obtain information on the correlation lengths, which is a measure of the average size of domains along the same direction in real space.

Molecular-dynamics simulations

Canonical-ensemble (NVT) molecular-dynamics simulations of PMN-PT were conducted for a $72 \times 72 \times 72$ perovskite-type supercell with 500 ps equilibrium run and 2 ns production time using a bond-valence-based interatomic potential. The temperature was controlled by the Nosé–Hoover thermostat with a thermal inertia parameter $M_s = 0.0207$ atomic mass unit (amu). The distribution of B cations and potentials was the same as those used in another work[15]. The lattice parameters for the 0.75% strain state were $a = b = 28.7784$ nm with $c/a = 1.0164$. The instantaneous local polarization, $\mathbf{P}_u(t)$, for each unit cell is calculated as $\mathbf{P}_u(t) = \frac{1}{V_u} \left(\frac{1}{8} \mathbf{Z}_A^* \sum_{i=1}^{8} \mathbf{r}_{A,i}(t) + \mathbf{Z}_B^* \mathbf{r}_B(t) + \frac{1}{2} \mathbf{Z}_O^* \sum_{i=1}^{6} \mathbf{r}_{O,i}(t) \right)$, where V_u is the volume of a unit cell and $\mathbf{Z}_A^*$, $\mathbf{Z}_B^*$ and $\mathbf{Z}_O^*$ are the Born effective charges of the A-site, B-site and oxygen atoms, respectively. Also, $\mathbf{r}_{A,i}(t)$, $\mathbf{r}_{B,i}(t)$ and $\mathbf{r}_{O,i}(t)$ are the instantaneous atomic positions of the A-site, B-site and oxygen atoms in a unit cell, respectively, as obtained from the molecular-dynamics simulations.

Computational-diffuse scattering. The computational diffuse-scattering patterns were calculated following the method employed elsewhere[20]. It should be noted that we do not apply pseudocubic symmetry in this work due to the tetragonal lattices induced by strain. Instead, we take the average of the calculated-diffuse scattering about the 002- and 00$\bar{2}$-diffraction conditions to remedy the roughly half-lengths of the c axis in our molecular-dynamics simulations compared with the experimental thickness of 55 nm.

Angle correlations. The time-delay-averaged angle correlation function (Supplementary Fig. 5a–j) is calculated as

$$\frac{1}{2N_c} \frac{1}{\sqrt{\pi\sigma}} \sum_{i=1}^{N_c} \sum_{j=1}^{2} \int e^{-\frac{(\theta - \theta_{ij}(t'))^2}{\sigma}} \, \mathrm{d}t', \quad (1)$$

where N_c is the number of lead atoms in PMN-PT, j denotes the target atoms in the nth neighbour cells along the $\pm x$, $\pm y$ and/or $\pm z$ directions from an origin lead atom, θ is a given angle, σ is the Gaussian width, t' is the time delay and θ_{ij} is the correlation function of the angle formed by displacements between the specific lead pairs above such that

$$\theta_{ij}(t') = \arccos \left(\int \hat{D}_i(t) \times \hat{D}_j(t + t') \, \mathrm{d}t \right), \quad (2)$$

where $\hat{D}(t)$ is the unit vector of a lead atom off-centring displacement as a function of time. The function is based on the data from another work[20], but we decompose the lead pairs into the in-plane and out-of-plane directions for better representation in this work. The autocorrelation of time-delay-averaged angles (Supplementary Fig. 5k–o) is the same as that elsewhere[20]:

$$\frac{1}{N_a} \frac{1}{\sqrt{\pi\sigma}} \sum_{i=1}^{N_a} \int e^{-\frac{(\theta - \theta_{ii}(t'))^2}{\sigma}} \, \mathrm{d}t', \quad (3)$$

where N_a is the number of lead atoms with values of 23,296, 93,151, 140,255, 93,349 and 23,197 for the subgroups $Pb(Mg_{1/2}Nb_{1/2})O_3$,

$Pb(Mg_{3/8}Nb_{1/2}Ti_{1/8})O_3$, $Pb(Mg_{1/4}Nb_{1/2}Ti_{1/4})O_3$, $Pb(Mg_{1/8}Nb_{1/2}Ti_{3/8})O_3$ and $Pb(Nb_{1/2}Ti_{1/2})O_3$, respectively.

STEM

PMN-PT thin films were prepared for STEM using a Ga$^+$ focused-ion beam (Thermo Fisher Scientific Helios 660) or mechanical polishing with final thinning using cryogenic argon-ion milling (Fischione 1051). For STEM imaging, a probe-aberration-corrected Thermo Fisher Scientific Themis Z microscope was operated at 200 kV with a probe convergence semi-angle of 18 mrad. The collection semi-angles for the simultaneously acquired ADF and iDPC were 25–153 and 6–24 mrad, respectively. The STEM images were acquired with the revolving STEM method to correct for distortion introduced by sample drift using 20 and 2,048 × 2,048 pixel frames with 90° rotation between each successive frame[38]. The sample thickness was 10–15 nm, determined using position-averaged convergent-beam electron diffraction[39]. The intensity and centroid of each atom column in the ADF and iDPC images were measured by fitting to 2D Gaussians using a custom Python 3.9 analysis tool. The projected polarization for each unit cell was calculated by taking the difference between the average column positions of the cation and anion from iDPC.

Data availability

All data supporting the findings of this study are available within the Article and its Supplementary Information. Additional data are available from the corresponding author upon request. Source data are provided with this paper.

Code availability

Custom Python scripts used to analyse the STEM images are available from the corresponding author upon request.

References

38. Sang, X. & LeBeau, J. M. Revolving scanning transmission electron microscopy: correcting sample drift distortion without prior knowledge. *Ultramicroscopy* **138**, 28–35 (2014).
39. LeBeau, J. M., Findlay, S. D., Allen, L. J. & Stemmer, S. Position averaged convergent beam electron diffraction: theory and applications. *Ultramicroscopy* **110**, 118–125 (2010).

Author contributions

J.K. and L.W.M. conceived this study. J.K. synthesized the films and performed the structural characterizations. J.K., A.F. and Z.T. fabricated the devices for *in operando* synchrotron diffraction. J.K. and D.M. performed the synchrotron diffraction measurements. A.K. and J.M.L. performed the STEM studies. Y.Q., H.T. and A.M.R. performed the molecular dynamics simulation studies. P.J.R. and J.-W.K. developed the *in operando* synchrotron diffraction setup. J.K., D.M., Z.T., P.J.R. and J.-W.K. performed the *in operando* synchrotron diffraction measurements. J.K. and A.K. wrote the initial draft of the manuscript. J.K., A.K., Y.Q., H.T., A.M.R., J.M.L. and L.W.M. revised the manuscript. All the authors discussed the results and edited the manuscript.

Competing interests

The authors declare no competing interests.

Additional information

Supplementary information The online version contains supplementary material available at
https://doi.org/10.1038/s41567-022-01773-y.

Correspondence and requests for materials should be addressed to Lane W. Martin.

Peer review information *Nature Physics* thanks Dawei Wang and the other, anonymous, reviewer(s) for their contribution to the peer review of this work.

Reprints and permissions information is available at www.nature.com/reprints.